Air pollution slows down surface warming over the Tibetan Plateau

Aolin Jia[1], Shunlin Liang[1], Dongdong Wang[1], Bo Jiang[2], Xiaotong Zhang[2]

[1]Department of Geographical Sciences, University of Maryland, College Park, MD, 20742, USA
[2]State Key Laboratory of Remote Sensing Science, Faculty of Geographical Science, Beijing Normal University, Beijing,
5 10085, China

Correspondence to: Shunlin Liang (sliang@umd.edu)

Abstract. The Tibetan Plateau (TP) plays a vital role in regional and global climate change. The TP has been undergoing significant surface warming since 1850, with an air temperature increase of 1.39 K and surface solar dimming resulting from decreased incident solar radiation. The causes and impacts of solar dimming on surface warming are unclear. In this study,

10 long-term (from 1850–2015) surface downward radiation datasets over the TP are developed by integrating 18 Coupled Model Intercomparison Project Phase 5 (CMIP5) models and satellite products. The validation results from two ground measurement networks show that the generated downward surface radiation datasets have higher accuracy than the mean of multiple CMIP5 and the fused datasets of reanalysis and satellite products. After analyzing the generated radiation data with four air temperature datasets, we found that downward shortwave radiation (DSR) remained stable before 1950 and then declined rapidly at a rate

15 of -0.53 W m^{-2} per decade and that the fastest decrease in DSR is in the southeastern TP. Evidence from site measurements, satellite observations, reanalysis, and model simulations suggested that TP solar dimming was primarily driven by increased anthropogenic aerosols. The TP solar dimming is stronger in summer, at the same time that the increasing magnitude of the surface air temperature is the smallest. The cooling effect of solar dimming offsets surface warming on the TP by 0.80 ± 0.28 K (48.6 ± 17.3%) in summer. It helps us understand the role of anthropogenic aerosols in climate warming, and highlights the

20 need for additional studies to be conducted to quantify the influence of air pollution on regional climate change over the TP.

1 Introduction

The Tibetan Plateau (TP), the so-called Third Pole, covers an area of approximately 2.65 × 10^2 km^2 and has an average elevation of more than 4000 m. It contains the largest ice mass outside of the polar regions (Yao et al., 2007) which supplies several major rivers that sustain billions of people in China and South Asia, dominating regional social stabilization and

25 development. The TP is a weak heat sink in winter but a strong heat source in summer and dominates the atmospheric circulation (Wu et al., 2015). The mechanical and thermal forcing of the large-scale orography is crucial for the formation of the Asian summer monsoon (Boos and Kuang, 2010) and water and heat exchange between the Pacific Ocean and Eurasia (Wu et al., 2012). The TP anticyclone transports water vapor and chemical gases into the lower stratosphere (Fu et al., 2006). Therefore, the local climate pattern over the TP plays a vital role in the climate in southern China (Xu et al., 2013), the boreal

30 climate (Sampe and Xie, 2010), and global climate change (Cai et al., 2017).

The TP is currently undergoing significant climate change (Yao et al., 2018), such as increased surface air temperature (Kuang and Jiao, 2016) and downward longwave radiation (DLR), as well as decreased downward solar radiation (DSR) (You et al., 2010) which is a solar dimming phenomenon that can impact surface temperatures (Wild et al., 2007) and precipitation (Wild, 2009). However, the causes of solar dimming over the TP are not yet conclusive (Kuang and Jiao, 2016;Xie and Zhu, 2013;Xie

35   et al., 2015). Changes in DSR are mainly controlled by atmospheric clouds and aerosols (Liang et al., 2010) at century-level scales. You et al. (2013) suggested that aerosols have played an important role in solar dimming over the TP in recent decades, while Tang et al. (2011) speculated that solar dimming over the TP might be caused by cloud cover changes that have a comparable influence on solar dimming to that of aerosol loading changes. Although some studies have suggested that brown clouds that are formed due to aerosols over the Indian Ocean and Asia (Ramanathan et al., 2007) might be transported to the

40   TP by the summer monsoon, Yang et al. (2012) and (2014) contended that the main drivers are deep convective clouds and atmospheric water vapor, and that aerosol radiative forcing is too small to result in the significantly decreased DSR over the TP. These studies clearly show contradictory conclusions regarding the proper attribution of the TP dimming; therefore, the roles of aerosols and clouds in TP dimming still need to be determined. Moreover, some of these studies were mainly based on ground measurements at a limited number of sites that cannot represent the entire TP. Furthermore, the surface observed

45   sunshine duration data that were used for estimating DSR (Wang, 2014;Yang et al., 2006) were not available over the TP until the 1960s. Regardless, the statistical model can hardly capture the low aerosols' influences on surface solar radiation by sunshine duration especially at complex terrains in TP. Thus, considering that remote sensing has been developed for several decades, it provides a valuable opportunity to employ satellite observations to monitor spatial temporal variations at regional scales.

50   The radiative effect of anthropogenic aerosols has not yet been well quantified by observations over the TP, and this information is necessary for understanding the role of anthropogenic aerosols in climate warming, and revealing impacts of human activities in remote areas. Calculating the radiative effect is vital for understanding the impact of aerosols on local and continental climate warming. Model simulations (Ji et al., 2015) have shown that carbonaceous aerosols have positive radiative forcing effects on climate warming over the TP, leading to a 0.1–0.5 °C warming in the monsoon season, while some studies

55   have demonstrated that anthropogenic aerosols (AAs) have a cooling effect on local climate warming (Smith et al., 2016;Sundström et al., 2015). Li et al. (2015) calculated the aerosol impact on climate warming in different seasons over arid-semiarid and humid-semiarid areas, and across China, and showed that China undergoes a cooling rate of −0.86 to −0.76 °C per century due to increased aerosols. However, these conclusions were based on model simulations (Liao et al., 2015) and have not yet been combined with observations.

60   In this study, calibrated by the Clouds and the Earth's Radiant Energy System Energy Balanced and Filled (CERES EBAF) Edition 4.0 surface downward radiation products (Kato et al., 2018), long-term (from 1850–2015) surface DSR and DLR datasets over the TP were developed by merging 18 Coupled Model Intercomparison Project Phase 5 (CMIP5) models (Taylor et al., 2012). Site validation and comparison were processed to the calibrated data, the CMIP5 model outputs, and other long-

term radiation products. The spatiotemporal variations in the generated surface radiation datasets and four long-term air
65 temperature datasets were initially analyzed, and the TP solar dimming was attributed by using multiple types of satellite and
reanalysis data, which were confirmed by climate model simulations. We characterized the seasonal difference of the TP solar
dimming and further quantified the depressing effect on local climate warming since 1850 using two methods driven by
satellite observations and model simulations.

2 Data and Methodology

70 ### 2.1 Data

2.1.1 Coupled Model Intercomparison Project Phase 5 (CMIP5) data

The CMIP5 (Taylor et al., 2012) datasets with spatial resolutions less than 2° were chosen in the paper, and 18 monthly
modeled datasets (summarized in Table 1) from the Historical experiment were included, which cover 1850 to 2005; the
following years (2006–2015) of records are from the Representative Concentration Pathway (RCP) 8.5 experiment. We used
75 the first ensemble (r1i1p1) only of each experiment to reduce the calibration complexity of surface downward radiation.
Aerosol optical depth, precipitation, and wind speed from the Historical and RCP8.5 experiments of the models were used to
analyze differences in dimming magnitudes at seasonal scales. Surface temperature, wind speed, and relative humidity were
employed for calculating the aerosol depressing effect due to the long-term coverage. The corresponding HistoricalMisc
experiment (i.e., an experiment that combined different specific forcings) data were also utilized in the attribution analysis,
80 including downward shortwave radiation driven by AA and noAA (all forcings except AA). The PiControl experiment
provided the natural internal variation utilized in the optimal fingerprinting method (Methodology 2.2.2). The attribution and
depressing effect calculation included all the available ensembles of each model. All datasets were resampled into 1 Lat/Lon
degree using a bilinear interpolation method. CMIP5 datasets are available from the Intergovernmental Panel on Climate
Change (IPCC) data distribution center at http://www.ipcc-data.org/sim/gcm_monthly/AR5/Reference-Archive.html (all data
85 were accessed on 15 December 2018).

2.1.2 Remote sensing and assimilation products

2.1.2.1 Clouds and the Earth's Radiant Energy System Energy Balanced and Filled (CERES EBAF) radiation products

The CERES EBAF-surface Edition 4.0 monthly downward shortwave and longwave radiation products (Kato et al., 2018)
were employed as a benchmark for calibrating simulated CMIP5 surface radiation by a non-negative least square (NNLS)
90 regression approach (Bro and De Jong, 1997) (Methodology 2.2.1). Comparing with former solar radiation products, CERES
EBAF has been comprehensively assessed and considered as the most advanced surface radiation satellite product. It is usually
used as a reference for model and reanalysis validation (Zhang et al., 2015;Zhang et al., 2016). Besides, former studies have
already used the CERES EBAF DSR product for applications and analysis (Feng and Wang, 2018;Ma et al., 2015). This new

version contains surface fluxes consistent with the top-of-atmosphere (TOA) fluxes provided from the CERES Energy
95 Balanced and Filled Top of Atmosphere (EBAF-TOA) data product. They also used improved cloud properties that are
corrected by cloud profiling radar, and consistent input sources are employed, such as temperature, humidity, and aerosol data,
in order to solve the spurious anomaly problem (Jia et al., 2018;Jia et al., 2016). All the advantages help to quantify the absolute
magnitude and temporal trend of surface DSR (Feng and Wang, 2019). The CERES EBAF-TOA Edition 4.0 monthly TOA
albedo product (Loeb et al., 2018) was used for computing the temporal variation in the TOA albedo over the Tibetan Plateau
100 (TP) in the dimming attribution analysis. The TOA solar radiation product was used as a monthly climatology and was
combined with the calibrated surface DSR data to compute the atmospheric shortwave transmissivity in the aerosol depressing
effect quantification. Meta information on the included products is summarized in Table 2. All products were pre-processed
into 1 degree at a monthly scale for further analysis to unify the spatial temporal resolution.

2.1.2.2 Aerosol, cloud, and dust products

105 Multiple aerosol, cloud, and dust products were employed for the attribution of solar dimming. The averages of the Moderate
Resolution Imaging Spectroradiometer (MODIS) MOD/MYD08 Collection 6.1 aerosol optical depth (AOD) 550 products that
combine the Dark Target and Deep Blue algorithms were used for detecting aerosol variations over the TP. The MOD/MYD08
C6.1 cloud fraction was also included in the attribution analysis. In MODIS C6.1, the brightness temperature biases and
trending were substantially reduced compared to C6, which affected the cloud retrieval and also caused large uncertainty with
110 respect to the AOD over elevated areas (Sogacheva et al., 2018). Additionally, the MODIS AOD coverage increased in C6.1.

The Sea-Viewing Wide Field-of-View Sensor (SeaWiFS) AOD550 product (Sayer et al., 2012) utilized 12 candidate aerosol
models for generating the aerosol lookup tables (Hsu et al., 2012), and AODs at different wavelengths have been retrieved
over land with the use of the Deep Blue algorithm (Pozzer et al., 2015). The SeaWiFS AOD550 product was used for
calculating the aerosol temporal variation over the TP.

115 The aerosol index data were inversed from Total Ozone Mapping Spectrometer (TOMS)-Nimbus 7, TOMS-Probe, and Ozone
Monitoring Instrument (OMI) at different time periods (Ahmad et al., 2006). We employed TOMS N7 records from 1980 to
1992, TOMS Probe from 1997 to 2004, and OMI from 2005 to 2015. By using the 340- and 380-nm wavelength channels
(which have negligible dependence on ozone absorption), the aerosol index was defined based on backscattered radiance
measured by TOMS and OMI and the radiance calculated from a radiative transfer model for a pure Rayleigh condition (Hsu
120 et al., 1999). This approach measures the relative amount of aerosols and has a comparable relationship with AOD (McPeters
et al., 1998).

Particulate matter (PM) 2.5, characterizing very small particles that have a diameter of < 2.5 µm and are produced by human
activities, is a common index of air pollution (Wang et al., 2015). We employed the PM2.5 satellite products to link the aerosol
loading with air pollution. The PM2.5 satellite product is calculated from MODIS, Multi-angle Imaging SpectroRadiometer

125   (MISR), and SeaWiFS AOD products based on a relationship generated from a chemical transport model (Van Donkelaar et al., 2016), and its uncertainty is determined by ground measurements.

MERRA2 aerosol products are the new generation reanalysis data that have assimilated MODIS and MISR land aerosol products since 2000 (Randles et al., 2017). Dust column mass density from MERRA2 was included for comparison of the temporal variation with PM2.5 data to determine whether the AOD increase was due to air pollution.

130   International Satellite Cloud Climatology Project (ISCCP) and Pathfinder Atmospheres–Extended (PATMOS-X) provide long-term cloud fraction products, however, the trend is spurious (Evan et al., 2007). This is because of the satellite zenith angle, equatorial crossing time, and because of the sensor calibration lack long-term stability. Corrected cloud fraction datasets (Norris and Evan, 2015), which were used for solar dimming attribution in this paper, employed an empirical method for removing artifacts from the ISCCP and PATMOS-X, and the corrected cloud products have been used for providing evidence

135   for climate change in satellite cloud records in other studies (Norris et al., 2016).

Diagnosing Earth's Energy Pathways in the Climate system (DEEP-C) TOA albedo was calculated by the DEEP-C monthly TOA absorbed solar radiation (ASR) (Allan et al., 2014) and monthly TOA incoming solar radiation climatology from the CERES EBAF-TOA Ed4.0 product. The DEEP-C TOA albedo was used for detecting the radiative influence of increasing aerosols in the dimming attribution. Central to the DEEP-C TOA radiation reconstruction are monthly observations of the

140   TOA radiation from the CERES scanning instruments after 2000 and Earth Radiation Budget Satellite (ERBS) wide field of view (WFOV) nonscanning instrument from 1985 to 1999. A strategy was required to homogenize the satellite datasets (Allan et al., 2014), and the European Centre for Medium-Range Weather Forecasts interim reanalysis (ERA-Interim) has provided atmospheric information since 1979, also using a subset of nine climate models to represent direct and indirect aerosol radiative forcings.

145   **2.1.2.3 Global LAnd Surface Satellite (GLASS) surface albedo product**

The GLASS surface albedo product provides ancillary data for calculating the aerosol depressing effect. The GLASS albedo product from MODIS observations is based on two direct albedo estimation algorithms (He et al., 2014); one designed for surface reflectance and one for TOA reflectance (Qu et al., 2014). The statistics-based temporal filtering fusion algorithm is used to integrate these two albedo products (Liu et al., 2013a). The GLASS albedo product has been assessed by ground

150   measurements and the MODIS albedo product and has comparable accuracy (Liu et al., 2013b).

2.1.2.4 Advanced Spaceborne Thermal Emission and Reflection Radiometer Global Monthly Emissivity Dataset (ASTER_GED)

The ASTER surface emissivity data were also used for calculating the aerosol depressing effect. The ASTER_GED data products are generated using the ASTER Temperature Emissivity Separation algorithm (Gillespie et al., 1998) atmospheric

155   correction method. This algorithm uses MODIS Atmospheric Profiles product MOD07 and the MODTRAN 5.2 radiative

transfer model, snow cover data from the standard monthly MODIS/Terra snow cover monthly global 0.05° product MOD10CM, and vegetation information from the MODIS monthly gridded NDVI product MOD13C2 (NASA JPL. ASTER Global Emissivity Dataset, 2016).

2.1.3 Ground measurements

160 Utilized for surface radiation validation, ground radiation measurement sites over the TP are mainly from two ground networks (Global Energy and Water Exchanges [GEWEX] Asian Monsoon Experiment [GAME] (Yasunari, 1994) and Coordinated Energy and Water Cycle Observation Project (CEOP) Asia-Australia Monsoon Project [CAMP] (Leese, 2001)) that cover 1995–2005. The China Meteorology Administration (CMA) network is not included due to a systematic error in the 1990s (Zhang et al., 2015). The GAME was proposed as an international project under the Global Energy and Water Exchanges

165 (GEWEX) program to understand the processes associated with the energy and hydrological cycle of the Asian monsoon system, and its variability. The data are available at http://www.hyarc.nagoya-u.ac.jp/game/phase-1/game-aan.html. The CAMP, which followed the GAME, focused on water and energy fluxes and reservoirs over specific land areas and monsoonal circulations. These data are available at http://metadata.diasjp.net/dmm/doc/CEOP_CAMP_Tibet-DIAS-en.html. We ignored the spatial representative difference between site observations and downward radiation datasets in line with former studies

170 (Wang and Dickinson, 2013;Zhang et al., 2015).

We also collected 5 sites from Global Energy Balance Archive (GEBA) over the TP to detect long-term temporal variation of surface DSR from 1960 to 2000. This ground measurement network is developed and maintained at ETH Zurich and the random error of DSR is 2% for annual means (Zhang et al., 2015). Even the site amount is not large enough to represent the whole TP, the sampled surface measurements can reflect the ground truth and support our conclusion. 22 sites that observed

175 downward radiation in the TP were included in this study, and their distribution is shown in Figure 1.

2.1.4 Surface air temperature datasets

Four long-term surface air temperature datasets were used for characterizing the temporal variation over the TP and corresponding aerosol depressing effect; the Berkley Earth Surface Temperature land surface air temperature dataset (BEST-LAND) (Rohde et al., 2013), Climate Research Unit Temperature Data Set version 4 (CRU-TEM4v) (Jones et al., 2012),

180 National Aeronautics and Space Administration Goddard Institute for Space Studies (NASA-GISS) (Hansen et al., 2010), and National Oceanic and Atmospheric Administration National Center for Environmental Information (NOAA-NCEI) (Smith et al., 2008). These data were interpolated and homogenized from ground observation networks. Rao et al. (2018) provided data assessment of the four air temperature datasets, and a brief summary of the datasets is provided in Supplementary Table S1.

2.2 Methodology

2.2.1 Calibration method

Long-term series surface downward radiation data are urgently needed for characterizing the spatial-temporal variation of surface radiation budget over the TP, and they are also essential for the solar dimming attribution and calculating the aerosol radiative forcing and depressing effect on the increasing air temperature. To generate a long-term series surface downward radiation data record with high accuracy, a non-negative least squares (NNLS) regression (Bro and De Jong, 1997) approach was employed for merging multiple CMIP5 model records. The non-negative multiple linear models are utilized because the non-negativity constraint of NNLS only applies a non-subtractive combination of all components (Eq. [1]).

$$y = \sum a_i x_i , (a_i \geq 0), \tag{1}$$

where y is the calibrated radiation data, a_i is the coefficient of each CMIP5 model simulation x_i.

The calibration was done pixel by pixel to avoid the influence of geolocation and elevation. Given that radiative fluxes are always positive, a key assumption here is that the CERES radiative flux can be expressed as a non-negative linear combination of each model output at each grid. One CMIP5 model may hardly present the variations in the actual radiative fluxes but should not have any negative contributions. To avoid the influence from the seasonal cycle on the expression of the inter-annual variation of the radiative flux, the fusion models were generated monthly. The CERES satellite products aid NNLS to provide the best-weighted combination for each CMIP5 model, producing improved validation results compared to those produced by only using the mean of all model outputs. Mean Bias Error (MBE), Root-Mean-Square-Error (RMSE), and R^2 were utilized for quantifying site validation and comparing with the mean CMIP5 data and multiple satellite and reanalysis product fused radiation data from Shi and Liang (2013). The temporal variation and comparison among products are calculated by using latitude-weighted average over the TP. Detailed description of assessment methods are introduced in Jia et al. (2018).

2.2.2 Attribution analysis

Optimal fingerprinting is a common method in the attribution analysis of model data. It is based on a linear relationship, and, if the scaling factor is > 0 at a certain significance level, the variable has a positive contribution toward the responding variable. The optimal fingerprinting method has been widely applied for climate change detection and attribution (Sun et al., 2014;Zhou et al., 2018). It is assumed that the response variable has a linear relationship with different driving variables (Eq. [2]):

$$y = \sum \beta_i x_i + \varepsilon, \tag{2}$$

where ε is the modeled natural internal variation obtained from the CMIP5 piControl Experiment, and β_i is the scaling factor of each driving variable x_i. If the scaling factor is > 0 at a certain significance level, the variable has a positive contribution toward the responding variable.

2.2.3 Depressing effect

For quantitating the depressing effect of aerosols on surface warming over the TP, the shortwave and longwave radiative effects must be separated. To calculate the relationship between the surface air temperature increase and surface radiation components, it is necessary to decompose the energy sources into separate mechanisms. The land surface energy balance is given by Eq. (3):

$$S_n + L_n = \lambda E + H + G, \tag{3}$$

where S_n is the net shortwave radiation, L_n is the net longwave radiation, λ is the latent heat of vaporization, E is evapotranspiration, H is the sensible heat flux, and G is the ground heat flux that was neglected for the long time period. They can be decomposed in Eq. (4) as:

$$S\tau(1 - \alpha) + \varepsilon_s \sigma (\varepsilon_a T_a^4 - T_s^4) = \lambda E + \rho C_d (T_s - T_a)/r_a, \tag{4}$$

where S is the TOA solar radiation, τ is the atmospheric shortwave transmissivity (ratio between the calibrated surface DSR and S), α is the surface albedo, ε_s is the surface emissivity, T_a is the air temperature, T_s is the surface skin temperature, and r_a is the aerodynamic resistance at 2 m height. σ is equal to 5.67×10^{-8} W m^{-2} K^{-4}, ρ is 1.21 kg m^{-3}, and C_d is 1013 J kg^{-1} K^{-1}. Considering that the ΔT_a is mainly dominated by the change in T_s interacting with T_a through radiative and thermal processes and the change in atmospheric circulation (ΔT_a^{cir}, for example, advection of cold and warm air masses), a first-order approximation of the direct near-surface temperature response to each component (Zeng et al., 2017) is derived from Eq. (5) and Eq. (6):

$$\Delta T_a = 1/f \, (S(1 - \alpha)\Delta\tau - S\tau\Delta\alpha - \lambda E + \varepsilon_s \sigma T_a^4 \Delta\varepsilon_a$$

$$+ \rho C_d((T_s - T_a)/r_a^2)\Delta r_a) + \Delta T_a^{cir}, \tag{5}$$

where the f is:

$$f = \rho C_d/r_a + 4\varepsilon_s \sigma \varepsilon_a T_a^3, \tag{6}$$

and f^{-1} represents the land surface air temperature sensitivity to 1 W m^{-2} radiative forcing at the land surface. We assumed that S, λ, ρ, C_d, σ, and ε_s are independent of T_s. We employed the α, ε_s, and S climatologies and the mean values of the satellite products for several years. Therefore, the T_a response to the surface DSR change is calculated by the first term (related to $\Delta\tau$) in the formula. Based on Eq. (7):

$$\text{DLR} = \sigma \varepsilon_a T_a^4, \tag{7}$$

from Eq. (8) we can also obtain the relationship between ΔT_a and ΔDLR:

$$\Delta T_a^{DLR} = \Delta\text{DLR}/(4\sigma \varepsilon_a T_a^3). \tag{8}$$

We then added the depressing effect from ΔDSR and ΔDLR to get the aerosol depressing effect on the TP climate warming. Although the first-order approximation method included many remote sensing products and had more reliable input than the model calculation, it ignored the heat exchange with surrounding areas. Hence, we also calculated the depressing effect of AAs by employing the CMIP5 air temperature data from multiple noAA simulations, which computed the influence of the interaction with other regions. We then compared the two results (Supplementary Fig. S5) and calculated the mean value as the final depressing effect result.

3 Results and discussion

3.1 Validation and comparison of the calibrated downward radiation data

From January 1995 to December 2005, in situ observations were collected at 17 sites for monthly validation of DSR and DLR. The scatter diagrams and validation results of the CERES calibrated data, mean CMIP5, and reanalysis and satellite fused product from Shi and Liang (2013) at two networks are shown in Figure 2.

Figure 2 indicates that the CERES calibrated datasets have the lowest bias and RMSE for DSR and DLR validation at GAME and CAMP network, and the R^2 at CAMP network has the highest. The bias of the calibrated DSR at CAMP (GAME) is -0.27 (-3.68) Wm^{-2} and the RMSE is 20.59 (25.27) Wm^{-2}, whereas the bias of calibrated DLR at CAMP (GAME) is 0.63 (-4.31) Wm^{-2} and the RMSE is 11.90 (21.08) Wm^{-2}. We can conclude that by using the NNLS method, the CERES calibration decreased the data bias and RMSE and improved the R^2, providing the best-weighted combination for each CMIP5 model and producing better validation results than those produced by only using the mean of all model outputs and data from former studies. The minor validation difference between the two networks is the system bias mainly caused by disparate instruments. We ignored the spatial mismatch between site observations and downward radiation datasets in line with former studies (Wang and Dickinson, 2013;Zhang et al., 2015). Moreover, the annual anomaly temporal variation was compared with the data from Shi and Liang (2013) and is shown in Figure 3.

The annual temporal variation illustrates that two products have a similar temporal trend of DSR and DLR at a decadal scale over the TP, and that the CERES calibrated data have longer time spans. The DSR output shown by Shi and Liang (2013) has a slightly larger decreasing trend, which may be because GEWEX and ISCCP surface radiation products have high weights in the model, and the related spurious cloud trend causes an overestimated dimming trend (Evan et al., 2007). Feng and Wang (2018) utilized a cumulative probability density function-based method to fuse CERES and longer time reanalysis surface DSR data, however in this study they only calibrated individual reanalysis whereas in the present study we merged multiple CMIP5 data that cover longer time span and include more climate general model simulations. Besides, most reanalysis did not include aerosol variation information, which is important to determine the DSR decadal variation and characterize the aerosol radiative forcing.

3.2 Characterizing long-term variations in air temperature and surface downward radiation over the Tibetan Plateau

Air temperatures slowly increased from 1850 to 2015. The DLR increased gradually prior to 1970 but rapidly during the following period. The DSR remained stable and decreased rapidly afterward, revealing an opposite trend to the DLR and air temperature (Figure 4a). In total, DSR decreased by 4.1 W m^{-2} from 1850 to 2015 with a gradient of -0.53 W m^{-2} per decade
275   after 1950, and DLR increased from 0.21 W m^{-2} per decade to 1.52 W m^{-2} per decade after 1970. Air temperature has increased by 1.39 K since 1850. Prior to 1950, increased air temperature was mainly triggered by increased DLR. Air temperature slightly decreased from 1950 to 1970, because both DSR and DLR decreased during that period. Although DLR increased rapidly after 1970, the air temperature gradient has not considerably changed, mainly due to solar dimming compressing the greenhouse effect. The solar dimming over TP is also detected by long-term ground DSR observations from 5 GEBA sites since 1960
280   (Supplementary Fig. S1) when the measurements were set up. Because heat exchange with other regions in the summer and winter are mostly counteracted, we ignored the interaction at decadal scales and suggested that air temperature is mainly driven by local radiation components. All four surface air temperature datasets show similar temporal trends, especially on the decadal scale.

The long-term spatiotemporal variations in downward surface radiation over the TP and surrounding regions are illustrated in
285   Figure 4b and 4c. Figure 4b demonstrates that the DSR decrease rate in the central region is about -0.08 W m^{-2} per decade, much lower than in surrounding areas. The fastest decrease in DSR appears in the southeastern TP at a gradient of about -0.37 W m^{-2} per decade since 1850. Northern India, South Asia, and southern China show a substantially dimming trend with a gradient of about -0.65 W m^{-2} per decade. The DLR has increased, especially in the central and northern TP (Figure 4c). However, the rate of increase is much slower in the southern and southeastern TP, with a gradient of approximately 0.21 W
290   m^{-2} per decade.

3.3 Attribution to the Tibetan Plateau solar dimming

3.3.1 Analysis of satellite products and reanalysis

Both observed satellite products and reanalysis datasets provide evidence that AAs are the major driver of the significant decrease in the DSR over the TP. The aerosol optical depth (AOD) products from the SeaWiFS (Sayer et al., 2012) and MODIS
295   08 C6.1 (Levy et al., 2007) satellite products demonstrated similar annual anomalies and increasing trends after 1998 (Figure 5a). The aerosol index, which measures the relative amount of aerosols and has a comparable relationship with AOD (McPeters et al., 1998), shows that the number of aerosols has been escalating over the past 30 years (Figure 5a). The AOD has increased 0.0098 over the TP based on the trend, causing approximately 1.97 Wm^{-2} of dimming since 1998, according to multiple CMIP5 AA simulations over the TP and near linear relationship between AOD and radiative forcing at this magnitude level (Yang et
300   al., 2012). This is larger than the calibrated DSR dimming result of 1.10 Wm^{-2}, and some of the dimming caused by the aerosol increase is offset by decreased cloud cover (Figure 5c).

The PM2.5 satellite product (Van Donkelaar et al., 2015) also showed an increasing trend after 2000 (Figure 5b), while MERRA2 dust loading (Randles et al., 2017), which has been assimilated from MODIS and MISR land aerosol products since 2000, has been decreasing. Particulate matter (PM) 2.5, characterizing very small particles that have a diameter of less than

305   2.5 micrometers and are produced by human activities, is a common index for measuring air pollution (Wang et al., 2015). The variation in PM2.5 and dust indicates that increased aerosols are mainly from air pollution rather than from natural causes.

Based on the corrected cloud fraction datasets (Norris and Evan, 2015) from the ISCCP and Pathfinder Atmospheres–Extended (PATMOS-X) and the average cloud fraction from MOD/MYD08 C6.1, the results demonstrate that the cloud fraction over the TP has been decreasing since 1980 (Figure 5c), indicating a trend opposite to the TP solar dimming. The overall temporal

310   variation of TOA albedo from DEEP-C (Allan et al., 2014) and CERES presents an increasing trend with a magnitude of ~0.01 over the TP from 1985 to 2015 (Figure 5d). The TOA albedo is an important component of Earth's energy budget and is mainly influenced by clouds and aerosols. It can be inferred that aerosols over the TP were recently increasing, reflecting more solar radiation into space and causing the TOA albedo increase and solar dimming at the surface.

Yang et al. (2012) argued that aerosols had limited radiative forcing compared with the DSR decrease over the TP, however,

315   ground observations used in these studies were only from one AErosol RObotic NETwork (AERONET) site at the center of the TP (30.773 °N, 90.962 °E). Furthermore, the site was less impacted by surrounding regions and so cannot represent the entire TP, especially the edge regions that are more easily contaminated by air pollution from surrounding areas.

Yang et al. (2012) and (2014) also suggested that the increasing trend in the deep convective clouds were attributed to the TP dimming, however, our analysis has different conclusion. We used the cloud top pressure and cloud optical depth released by

320   MODIS at different atmospheric levels to detect which pixels are deep convective clouds. The threshold is based on the definition of ISCCP (Rossow and Schiffer, 1999). Then, we calculated the ratio of deep convective clouds in all pixels over the TP and obtained the temporal variation and spatial distribution. Moreover, regardless of cloud type, the cloud mainly affects the DSR by cloud optical depth, so we reviewed the temporal variation of the total cloud optical depth. The analysis illustrates that even though the ratio of deep convective clouds is increasing (Supplementary Fig. S2a), deep convective clouds only

325   appeared in the south and west of the TP (Supplementary Fig. S2b). Additionally, the overall cloud optical depth has been decreasing over the past 15 years (Supplementary Fig. S2a). Therefore, deep convective clouds have little influence over the entire TP.

We also assessed the temporal variation of the atmospheric water vapor and total column water vapor (Supplementary Fig. S3), suggested as an important driving factor of TP dimming by Yang et al. (2012), and the temporal variation illustrated that

330   water vapor has been decreasing since 1998 over the TP. However, solar dimming did not show a similar turning point around 1998, and rather the overall increasing trend of water vapor since 1980 was limited. Therefore, the influence of water vapor variations can be ignored. The Yang et al. (2012) study also identified this phenomenon by using ECMWF Re-Analysis (ERA)-40, however, this research ceased in 2005 and did not show an overall turning trend.

Although satellite products analysis only began in 1980, observational records have existed for more than 30 years, and the
335   spatial extent of the satellite data over the entire TP supports our conclusions. Figure 4b shows that the regions of China, India,
and South Asia surrounding the TP have large populations and serious air pollution. Balloon-borne observations (Tobo et al.,
2007) and remote sensing products (Vernier et al., 2015) have shown that fine aerosols can be transported over the TP region
and enter the Asian tropopause aerosol layer by deep convection via two key pathways over heavily polluted regions (Lau et
al., 2018). Because of the decreasing dust amount trend the TP, we infer that the increased aerosols are mainly due to air
340   pollution around the TP. Although TP is still one of the cleanest areas in the world and the aerosol climatology is low, the
dimming can be demonstrated by the variation of DSR decadal anomalies. It is necessary to point out that direct radiative
effects (scattering and absorption effect) play a dominant role in the interactions between aerosols and the atmosphere (Li et
al., 2017) when the aerosol loading is low. Thus TP is easily affected by the aerosols increase under a clean atmosphere
condition.

345

3.3.2 Analysis of model simulations

The long-term model simulation results also show that AAs are the main driving factor of solar dimming. Based on the multiple
CMIP5 HistoricalMisc (an experiment combining different specific forcings) model ensembles, we found that the calibrated
DSR and the DSR driven by AAs and noAA had stable variations before 1950. The calibrated DSR obviously decreased after
350   1950 (Figure 6a). Only the AA-driven DSR can capture the dimming trend since 1950, therefore we can conclude that AAs
are the main signal at the decadal scale, while the factors in the noAA-driven model process (such as cloud cover and water
vapor) can be ignored. We also detected the AA and noAA driving factors using the optimal fingerprint method, and observed
that AAs had a positive contribution, especially after 1970 (Figure 6b). The impact factor of noAA is negative, and the satellite
cloud products reveal the same conclusion after 1980 (Figure 5c), i.e., that the cloud fraction has been decreasing and has had
355   a negative contribution to the TP solar dimming. Therefore, the attribution results from model simulations match the evidence
from the satellite data very well.

General climate models have coarser spatial resolution, causing the elevation in the model is lower than the reality and this
may cause higher AOD estimation over highland area. However, when we compared the multiple CMIP5 AOD with site
measurements, it demonstrates that the overall magnitude and monthly variation of CMIP5 AOD match the AERONET
360   observations (Supplementary Fig. S4), even though it is slightly higher than the AOD in the non-monsoon season. Therefore,
it is reasonable to include the CMIP5 AA and noAA simulations in the attribution work. Results of multiple models have
uncertainties, which are illustrated as colored shadow, but the overall variation is of significance tested in temporal analysis
and optimal fingerprint method.

3.4 Depressing effects of aerosols on climate warming in summer

365   By comparing the first 30 years of climatology (1850–1880) and the last 30 years of climatology (1985–2015), we found that the TP solar dimming is stronger in summer (from June to August), at the same time that the increasing magnitude of the surface air temperature is the smallest (Figure 7a). Multiple CMIP5 model ensembles show that changes in precipitation and wind speed over the TP during different seasons were related to the AOD increase. Precipitation in summer had the greatest decrease relative to other seasons, while AOD increased more in the summer (Figure 7b). Furthermore, the wind speed clearly

370   decreased in summer compared to other seasons (Figure 7c). TP is a strong heat source in summer, forming a sensible heat–derived air-pump that dominates the atmospheric circulation (Wu et al., 2015) and conveys aerosols into the lower stratosphere (Lau et al., 2018). However, increased precipitation will reduce the aerosol duration lifetime considerably (Liao et al., 2015), and wind speed also controls aerosol diffusion. Hence it is evident that less precipitation and lower wind speeds in summer resulted in greater aerosol stability.

375   Although aerosols have considerably influenced summer downward radiation over the TP, their radiative effect on climate warming has not been quantitatively calculated. By employing the multiple noAA model simulations, the temporal variation of aerosol radiative forcing over the TP are illustrated in the Supplementary Fig. S5. It demonstrates that the aerosol radiative forcing has been increasing about 8.08 Wm^{-2} by calculating the difference between the first 30 years of climatology (1850–1880) and the last 30 years of climatology (1985–2015).

380   Quantification of the depressing effect from AAs is essential for evaluating the impact of air pollution on local and continental climate warming and is also vital for improving our understanding of the role of human activities in remote areas. The depressing effects of aerosols on air temperature in summer (Figure 8) were calculated using two methods: one is using first-order approximations of the direct near-surface air temperature response to each radiative and thermodynamic component and is based on remote sensing and modeling data; the other is calculated by using multiple noAA simulations. The two methods

385   had similar depressing magnitudes (Supplementary Fig. S6), and the mean is shown in Figure 8. Surface air temperature increased almost 0.86 K (Figure 7a) over the TP in summer when comparing the first 30 years and the last 30 years, whereas the increasing magnitude of the surface air temperature that has no aerosol impact (the red line in Figure 8) is approximately 1.64 ± 0.28 K, which indicates that approximately 0.80 ± 0.28 K (48.6 ± 17.3%) of the local climate warming over the TP has been depressed by aerosols since 1850 in summer.

390   The first-order approximation method utilized many remote sensing products as climatology and forcing input, which are more reliable than the model simulations, but it ignored the heat exchange with surrounding areas. Hence, we also calculated the depressing effect of AAs by employing the CMIP5 air temperature data from multiple noAA simulations, which computed the influence of the interaction with other regions. Then we calculated the mean value as the final depressing effect result for including the advantages of these two methods.

4 Conclusion

The TP plays a vital role in regional and global climate change due to its location and orography. Former studies have proven that this region undergoes significant climate change, however, the causes and impacts of solar dimming are still under debate. Calibrated by the CERES EBAF surface downward radiation products and using NNLS method, long-term (from 1850–2015) surface DSR and DLR datasets over the TP were developed by merging 18 CMIP5 models. Compared with the mean of multiple CMIP5 data and fusion data from former studies, the CERES calibrated data had the lowest bias and RMSE for DSR and DLR validation at GAME and CAMP network, and the highest R^2 at CAMP network. The calibrated DSR and DLR have similar temporal trends over the TP at a decadal scale compared to the fusion of multiple reanalysis and satellite products.

Based on calibrated surface downward radiation data and four sets of air temperature data, we characterized the spatiotemporal variation in surface radiation along with temperature. The TP is currently experiencing substantial climate warming and solar dimming at the surface. In total, DSR decreased by 4.1 W m^{-2} from 1850 to 2015 with a gradient of -0.53 W m^{-2} per decade after 1950, and DLR increased from 0.21 W m^{-2} per decade to 1.52 W m^{-2} per decade after 1970. Air temperature has increased by 1.39 K since 1850. The dimming is also detected from long-term observing GEBA sites. Spatial and temporal analyses illustrated that the DSR decrease rate in the central region was approximately -0.08 W m^{-2} per decade, much lower than in surrounding areas. The fastest decrease in DSR appeared in the southeastern TP at a gradient of about -0.37 W m^{-2} per decade since 1850, and DLR has increased, especially in the central and northern TP. However, the rate of increase is much slower in the southern and southeastern TP, with gradients of approximately 0.21 W m^{-2} per decade.

By employing satellite and reanalysis products of aerosols, PM2.5, dust, cloud fractions, and TOA albedo, we determined that anthropogenic aerosols were the main cause of the solar dimming over the TP. The aerosol optical depth and the aerosol index has increased since the 1980s over the TP and increasing PM2.5 and decreasing dust linked the increasing aerosol to air pollution. We also proved from satellite products and reanalysis data that deep convective cloud and atmospheric water vapor are not the main drivers, due to limited distribution and magnitude since the 1980s. Furthermore, the overall cloud optical depth is decreasing. Additional evidence from multiple CMIP5 HistoricalMisc experiment ensembles also supports this conclusion that anthropogenic aerosols were the main cause of solar dimming over the TP.

Solar dimming over the TP is stronger in summer when the increasing magnitude of the surface air temperature is the smallest. Decreased precipitation and wind speeds triggered increased aerosol stability. Comparing the averages of the first 30 years (1850–1880) and last 30 years (1985–2015), the surface air temperature increased by approximately 0.86 K over the TP in the summer. Relying on calculated aerosol radiative forcings, the depressing effect of aerosol was calculated using two methods and both of which showed similar depressing magnitude. The increasing magnitude of the surface air temperature (with no aerosol impact) was approximately 1.58 K, which means approximately 0.80 ± 0.28 K ($48.6 \pm 17.3\%$) of the local climate warming over the TP has been depressed by aerosols since 1850 in summer. The study reveals the impacts of human activities on regional warming, even in remote areas, and highlights the need for additional studies to be conducted to quantify the

influence of air pollution on regional climate change over the TP. Therefore, we will focus on the influences of air pollution on local precipitation over the TP and surrounding areas in the next work.

Author contributions

430   S. Liang conceived and scoped the research. A. Jia, B. Jiang, and X. Zhang downloaded and pre-processed the data. A. Jia and D. Wang performed data statistics and the interpretation of the results. A. Jia and S. Liang wrote the manuscript. All authors contributed to revising the article.

Acknowledgments

This study was supported by NASA under grant 80NSSC18K0620 and the Chinese Grand Research Program on Climate
435   Change and Response (projects 2016YFA0600101 and 2016YFA0600103). We gratefully acknowledge the Intergovernmental Panel on Climate Change (IPCC) data distribution center for providing the model simulation outputs. We also thank the CERES science team, MODIS science team, Goddard Earth Sciences Data and Information Services Center (GES DISC), Earth Observing System Data and Information System (EOSDIS), Atmospheric Composition Analysis Group at Dalhousie University, Research Data Archive at the National Center for Atmospheric Research (NCAR), GLASS science team, and Land
440   Processes Distributed Active Archive Center (LP DAAC) for providing satellite and reanalysis products. We acknowledge the Berkeley Earth, Goddard Institute for Space Studies, National Centers for Environmental Information, and Climate Research Unit for providing near-surface air temperature datasets. We also thank the GEWEX Asian Monsoon Experiment (GAME), CEOP Asia-Australia Monsoon Project, and Aerosol Robotic Network for providing ground measurements.

Data and code availability

445   The authors declare that the data we generated will be available after acceptance. All datasets supporting the findings of this study were identified by referring citations in the references section. Analysis scripts are available by request to S. Liang.

Competing financial interests

The authors declare no competing financial interests.

References

450   Ahmad, S. P., Torres, O., Bhartia, P., Leptoukh, G., and Kempler, S.: Aerosol index from TOMS and OMI measurements, Proc. of the 86th AMS annual meeting, 2006,

Allan, R. P., Liu, C., Loeb, N. G., Palmer, M. D., Roberts, M., Smith, D., and Vidale, P. L.: Changes in global net radiative imbalance 1985–2012, Geophysical research letters, 41, 5588-5597, 2014.

Boos, W. R., and Kuang, Z. M.: Dominant control of the South Asian monsoon by orographic insulation versus plateau heating, Nature, 463, 218-U102, 10.1038/nature08707, 2010.

Bro, R., and De Jong, S.: A fast non-negativity-constrained least squares algorithm, Journal of Chemometrics: A Journal of the Chemometrics Society, 11, 393-401, 1997.

Cai, D. L., You, Q. L., Fraedrich, K., and Guan, Y. N.: Spatiotemporal Temperature Variability over the Tibetan Plateau: Altitudinal Dependence Associated with the Global Warming Hiatus, Journal of Climate, 30, 969-984, 10.1175/Jcli-D-16-0343.1, 2017.

Dufresne, J.-L., Foujols, M.-A., Denvil, S., Caubel, A., Marti, O., Aumont, O., Balkanski, Y., Bekki, S., Bellenger, H., and Benshila, R.: Climate change projections using the IPSL-CM5 Earth System Model: from CMIP3 to CMIP5, Climate Dynamics, 40, 2123-2165, 2013.

Evan, A. T., Heidinger, A. K., and Vimont, D. J.: Arguments against a physical long-term trend in global ISCCP cloud amounts, Geophysical Research Letters, 34, 2007.

Feng, F., and Wang, K.: Merging satellite retrievals and reanalyses to produce global long-term and consistent surface incident solar radiation datasets, Remote Sensing, 10, 115, 2018.

Feng, F., and Wang, K.: Determining factors of monthly to decadal variability in surface solar radiation in China: evidences from current reanalyses, Journal of Geophysical Research: Atmospheres, 2019.

Franklin, C. N., Sun, Z., Bi, D. H., Dix, M., Yan, H. L., and Bodas-Salcedo, A.: Evaluation of clouds in ACCESS using the satellite simulator package COSP: Regime-sorted tropical cloud properties, J Geophys Res-Atmos, 118, 6663-6679, 10.1002/jgrd.50496, 2013.

Fu, R., Hu, Y., Wright, J. S., Jiang, J. H., Dickinson, R. E., Chen, M., Filipiak, M., Read, W. G., Waters, J. W., and Wu, D. L.: Short circuit of water vapor and polluted air to the global stratosphere by convective transport over the Tibetan Plateau, Proc Natl Acad Sci U S A, 103, 5664-5669, 10.1073/pnas.0601584103, 2006.

Gent, P. R., Danabasoglu, G., Donner, L. J., Holland, M. M., Hunke, E. C., Jayne, S. R., Lawrence, D. M., Neale, R. B., Rasch, P. J., Vertenstein, M., Worley, P. H., Yang, Z. L., and Zhang, M. H.: The Community Climate System Model Version 4, Journal of Climate, 24, 4973-4991, 10.1175/2011jcli4083.1, 2011.

Gillespie, A., Rokugawa, S., Matsunaga, T., Cothern, J. S., Hook, S., and Kahle, A. B.: A temperature and emissivity separation algorithm for Advanced Spaceborne Thermal Emission and Reflection Radiometer (ASTER) images, IEEE transactions on geoscience and remote sensing, 36, 1113-1126, 1998.

GLOBE, T.: Team and others (Hastings, David A., Paula K. Dunbar, Gerald M. Elphingstone, Mark Bootz, Hiroshi Murakami, Hiroshi Maruyama, Hiroshi Masaharu, Peter Holland, John Payne, Nevin A. Bryant, Thomas L. Logan, J.-P. Muller, Gunter Schreier, and John S. MacDonald), eds., 1999, The Global Land One-kilometer Base Elevation (GLOBE) Digital Elevation Model, Version, 1, 80305-83328,

Gordon, H. B., O'Farrell, S., Collier, M., Dix, M., Rotstayn, L., Kowalczyk, E., Hirst, T., and Watterson, I.: The CSIRO Mk3. 5 climate model, CSIRO and Bureau of Meteorology, 2010.

Hansen, J., Ruedy, R., Sato, M., and Lo, K.: Global surface temperature change, Reviews of Geophysics, 48, 2010.

He, T., Liang, S., and Song, D. X.: Analysis of global land surface albedo climatology and spatial-temporal variation during
490   1981–2010 from multiple satellite products, Journal of Geophysical Research: Atmospheres, 119, 10,281-210,298, 2014.

Hsu, N., Gautam, R., Sayer, A., Bettenhausen, C., Li, C., Jeong, M., Tsay, S., and Holben, B.: Global and regional trends of aerosol optical depth over land and ocean using SeaWiFS measurements from 1997 to 2010, 2012.

Hsu, N. C., Herman, J., Torres, O., Holben, B., Tanre, D., Eck, T., Smirnov, A., Chatenet, B., and Lavenu, F.: Comparisons of the TOMS aerosol index with Sun-photometer aerosol optical thickness: Results and applications, Journal of Geophysical
495   Research: Atmospheres, 104, 6269-6279, 1999.

Ji, Z. M., Kang, S. C., Cong, Z. Y., Zhang, Q. G., and Yao, T. D.: Simulation of carbonaceous aerosols over the Third Pole and adjacent regions: distribution, transportation, deposition, and climatic effects, Climate Dynamics, 45, 2831-2846, 10.1007/s00382-015-2509-1, 2015.

Jia, A., Jiang, B., Liang, S., Zhang, X., and Ma, H.: Validation and Spatiotemporal Analysis of CERES Surface Net Radiation
500   Product, Remote Sensing, 8, 90, 2016.

Jia, A., Liang, S., Jiang, B., Zhang, X., and Wang, G.: Comprehensive Assessment of Global Surface Net Radiation Products and Uncertainty Analysis, Journal of Geophysical Research Atmospheres, 2018.

Jones, P., Lister, D., Osborn, T., Harpham, C., Salmon, M., and Morice, C.: Hemispheric and large-scale land-surface air temperature variations: An extensive revision and an update to 2010, Journal of Geophysical Research: Atmospheres, 117,
505   2012.

Jungclaus, J. H., Lorenz, S. J., Timmreck, C., Reick, C. H., Brovkin, V., Six, K., Segschneider, J., Giorgetta, M. A., Crowley, T. J., Pongratz, J., Krivova, N. A., Vieira, L. E., Solanki, S. K., Klocke, D., Botzet, M., Esch, M., Gayler, V., Haak, H., Raddatz, T. J., Roeckner, E., Schnur, R., Widmann, H., Claussen, M., Stevens, B., and Marotzke, J.: Climate and carbon-cycle variability over the last millennium, Clim Past, 6, 723-737, 10.5194/cp-6-723-2010, 2010.

510   Kato, S., Rose, F. G., Rutan, D. A., Thorsen, T. J., Loeb, N. G., Doelling, D. R., Huang, X., Smith, W. L., Su, W., and Ham, S.-H.: Surface irradiances of edition 4.0 Clouds and the Earth's Radiant Energy System (CERES) Energy Balanced and Filled (EBAF) data product, Journal of Climate, 31, 4501-4527, 2018.

Kuang, X. X., and Jiao, J. J.: Review on climate change on the Tibetan Plateau during the last half century, J Geophys Res-Atmos, 121, 3979-4007, 10.1002/2015jd024728, 2016.

515   Lau, W. K. M., Yuan, C., and Li, Z.: Origin, Maintenance and Variability of the Asian Tropopause Aerosol Layer (ATAL): The Roles of Monsoon Dynamics, Sci Rep, 8, 3960, 10.1038/s41598-018-22267-z, 2018.

Leese, J. A.: Coordinated Enhanced Observing Period (CEOP) Implementation Plan, International GEWEX Project Office, 2001.

Levy, R. C., Remer, L., Mattoo, S., Vermote, E., and Kaufman, Y.: Second-generation algorithm for retrieving aerosol
520 properties over land from MODIS spectral reflectance, J. Geophys. Res, 112, D13, 2007.

Li, C., Zhao, T., and Ying, K.: Effects of anthropogenic aerosols on temperature changes in China during the twentieth century based on CMIP5 models, Theoretical and Applied Climatology, 125, 529-540, 10.1007/s00704-015-1527-6, 2015.

Li, Z., Rosenfeld, D., and Fan, J.: Aerosols and their impact on radiation, clouds, precipitation, and severe weather events, in: Oxford Research Encyclopedia of Environmental Science, 2017.

525 Liang, S., Wang, K., Zhang, X., and Wild, M.: Review on estimation of land surface radiation and energy budgets from ground measurement, remote sensing and model simulations, Selected Topics in Applied Earth Observations and Remote Sensing, IEEE Journal of, 3, 225-240, 2010.

Liao, H., Chang, W., and Yang, Y.: Climatic effects of air pollutants over China: A review, Advances in Atmospheric Sciences, 32, 115-139, 2015.

530 Liu, N., Liu, Q., Wang, L., Liang, S., Wen, J., Qu, Y., and Liu, S.: A statistics-based temporal filter algorithm to map spatiotemporally continuous shortwave albedo from MODIS data, Hydrology and Earth System Sciences, 17, 2121-2129, 2013a.

Liu, Q., Wang, L., Qu, Y., Liu, N., Liu, S., Tang, H., and Liang, S.: Preliminary evaluation of the long-term GLASS albedo product, International Journal of Digital Earth, 6, 69-95, 2013b.

535 Loeb, N. G., Doelling, D. R., Wang, H. L., Su, W. Y., Nguyen, C., Corbett, J. G., Liang, L. S., Mitrescu, C., Rose, F. G., and Kato, S.: Clouds and the Earth's Radiant Energy System (CERES) Energy Balanced and Filled (EBAF) Top-of-Atmosphere (TOA) Edition-4.0 Data Product, Journal of Climate, 31, 895-918, 10.1175/Jcli-D-17-0208.1, 2018.

Long, M. C., Lindsay, K., Peacock, S., Moore, J. K., and Doney, S. C.: Twentieth-century oceanic carbon uptake and storage in CESM1 (BGC), Journal of Climate, 26, 6775-6800, 2013.

540 Ma, Q., Wang, K., and Wild, M.: Impact of geolocations of validation data on the evaluation of surface incident shortwave radiation from Earth System Models, Journal of Geophysical Research: Atmospheres, 120, 6825-6844, 2015.

McPeters, R. D., Bhartia, P., Krueger, A. J., Herman, J. R., Wellemeyer, C. G., Seftor, C. J., Jaross, G., Torres, O., Moy, L., and Labow, G.: Earth probe total ozone mapping spectrometer (TOMS): data products user's guide, 1998.

Meehl, G. A., Washington, W. M., Arblaster, J. M., Hu, A. X., Teng, H. Y., Kay, J. E., Gettelman, A., Lawrence, D. M.,
545 Sanderson, B. M., and Strand, W. G.: Climate Change Projections in CESM1(CAM5) Compared to CCSM4, Journal of Climate, 26, 6287-6308, 10.1175/Jcli-D-12-00572.1, 2013.

Mochizuki, T., Chikamoto, Y., Kimoto, M., Ishii, M., Tatebe, H., Komuro, Y., Sakamoto, T. T., Watanabe, M., and Mori, M.: Decadal Prediction Using a Recent Series of MIROC Global Climate Models, Journal of the Meteorological Society of Japan, 90a, 373-383, 10.2151/jmsj.2012-A22, 2012.

550 Norris, J. R., and Evan, A. T.: Empirical Removal of Artifacts from the ISCCP and PATMOS-x Satellite Cloud Records, Journal of Atmospheric and Oceanic Technology, 32, 691-702, 10.1175/jtech-d-14-00058.1, 2015.

Norris, J. R., Allen, R. J., Evan, A. T., Zelinka, M. D., O'dell, C. W., and Klein, S. A.: Evidence for climate change in the satellite cloud record, Nature, 536, 72-75, 2016.

Pozzer, A., De Meij, A., Yoon, J., Tost, H., Georgoulias, A., and Astitha, M.: AOD trends during 2001–2010 from observations and model simulations, Atmospheric Chemistry and Physics, 15, 5521-5535, 2015.

Qu, Y., Liu, Q., Liang, S., Wang, L., Liu, N., and Liu, S.: Direct-estimation algorithm for mapping daily land-surface broadband albedo from MODIS data, IEEE Transactions on Geoscience and Remote sensing, 52, 907-919, 2014.

Ramanathan, V., Ramana, M. V., Roberts, G., Kim, D., Corrigan, C., Chung, C., and Winker, D.: Warming trends in Asia amplified by brown cloud solar absorption, Nature, 448, 575, 2007.

Randles, C., Da Silva, A., Buchard, V., Colarco, P., Darmenov, A., Govindaraju, R., Smirnov, A., Holben, B., Ferrare, R., and Hair, J.: The MERRA-2 aerosol reanalysis, 1980 onward. Part I: System description and data assimilation evaluation, Journal of Climate, 30, 6823-6850, 2017.

Rao, Y., Liang, S., and Yu, Y.: Land surface air temperature data are considerably different among BEST-LAND, CRU-TEM4v, NASA-GISS, and NOAA-NCEI, Journal of Geophysical Research: Atmospheres, 2018.

Rohde, R., Muller, R., Jacobsen, R., Muller, E., Perlmutter, S., Rosenfeld, A., Wurtele, J., Groom, D., and Wickham, C.: A new estimate of the average Earth surface land temperature spanning 1753 to 2011. Geoinfor Geostat Overview 1: 1, of, 7, 2, 2013.

Rossow, W. B., and Schiffer, R. A.: Advances in understanding clouds from ISCCP, Bulletin of the American Meteorological Society, 80, 2261-2288, 1999.

Sampe, T., and Xie, S. P.: Large-Scale Dynamics of the Meiyu-Baiu Rainband: Environmental Forcing by the Westerly Jet, Journal of Climate, 23, 113-134, 10.1175/2009jcli3128.1, 2010.

Sayer, A., Hsu, N., Bettenhausen, C., Jeong, M., Holben, B., and Zhang, J.: Global and regional evaluation of over-land spectral aerosol optical depth retrievals from SeaWiFS, 2012.

Scoccimarro, E., Gualdi, S., Bellucci, A., Sanna, A., Giuseppe Fogli, P., Manzini, E., Vichi, M., Oddo, P., and Navarra, A.: Effects of tropical cyclones on ocean heat transport in a high-resolution coupled general circulation model, Journal of Climate, 24, 4368-4384, 2011.

Shi, Q., and Liang, S.: Characterizing the surface radiation budget over the Tibetan Plateau with ground-measured, reanalysis, and remote sensing data sets: 1. Methodology, Journal of Geophysical Research: Atmospheres, 118, 9642-9657, 2013.

Smith, D. M., Booth, B. B., Dunstone, N. J., Eade, R., Hermanson, L., Jones, G. S., Scaife, A. A., Sheen, K. L., and Thompson, V.: Role of volcanic and anthropogenic aerosols in the recent global surface warming slowdown, Nature Climate Change, 6, 936, 2016.

Smith, T. M., Reynolds, R. W., Peterson, T. C., and Lawrimore, J.: Improvements to NOAA's historical merged land–ocean surface temperature analysis (1880–2006), Journal of Climate, 21, 2283-2296, 2008.

Sogacheva, L., Leeuw, G. d., Rodriguez, E., Kolmonen, P., Georgoulias, A. K., Alexandri, G., Kourtidis, K., Proestakis, E., Marinou, E., and Amiridis, V.: Spatial and seasonal variations of aerosols over China from two decades of multi-satellite

observations–Part 1: ATSR (1995–2011) and MODIS C6. 1 (2000–2017), Atmospheric Chemistry and Physics, 18, 11389-11407, 2018.

Sun, Y., Zhang, X., Zwiers, F. W., Song, L., Wan, H., Hu, T., Yin, H., and Ren, G.: Rapid increase in the risk of extreme summer heat in Eastern China, Nature Climate Change, 4, 1082, 2014.

590 Sundström, A. M., Arola, A., Kolmonen, P., Xue, Y., de Leeuw, G., and Kulmala, M.: On the use of a satellite remote-sensing-based approach for determining aerosol direct radiative effect over land: a case study over China, Atmospheric Chemistry and Physics, 15, 505-518, 10.5194/acp-15-505-2015, 2015.

Tang, W.-J., Yang, K., Qin, J., Cheng, C., and He, J.: Solar radiation trend across China in recent decades: a revisit with quality-controlled data, Atmospheric Chemistry and Physics, 11, 393-406, 2011.

595 Taylor, K. E., Stouffer, R. J., and Meehl, G. A.: An overview of CMIP5 and the experiment design, Bulletin of the American Meteorological Society, 93, 485, 2012.

Tjiputra, J. F., Roelandt, C., Bentsen, M., Lawrence, D. M., Lorentzen, T., Schwinger, J., Seland, O., and Heinze, C.: Evaluation of the carbon cycle components in the Norwegian Earth System Model (NorESM), Geoscientific Model Development, 6, 301-325, 10.5194/gmd-6-301-2013, 2013.

600 Tobo, Y., Iwasaka, Y., Shi, G.-Y., Kim, Y.-S., Ohashi, T., Tamura, K., and Zhang, D.: Balloon-borne observations of high aerosol concentrations near the summertime tropopause over the Tibetan Plateau, Atmospheric Research, 84, 233-241, 10.1016/j.atmosres.2006.08.003, 2007.

Van Donkelaar, A., Martin, R. V., Brauer, M., and Boys, B. L.: Global Annual PM2. 5 Grids from MODIS, MISR and SeaWiFS Aerosol Optical Depth (AOD), 1998-2012, Palisades, NY: NASA Socioeconomic Data and Applications Center 605 (SEDAC). doi, 10, H4028PFS, 2015.

Van Donkelaar, A., Martin, R. V., Brauer, M., Hsu, N. C., Kahn, R. A., Levy, R. C., Lyapustin, A., Sayer, A. M., and Winker, D. M.: Global estimates of fine particulate matter using a combined geophysical-statistical method with information from satellites, models, and monitors, Environ Sci Technol, 50, 3762-3772, 2016.

Vernier, J. P., Fairlie, T. D., Natarajan, M., Wienhold, F. G., Bian, J., Martinsson, B. G., Crumeyrolle, S., Thomason, L. W., 610 and Bedka, K. M.: Increase in upper tropospheric and lower stratospheric aerosol levels and its potential connection with Asian pollution, J Geophys Res Atmos, 120, 1608-1619, 10.1002/2014JD022372, 2015.

Voldoire, A., Sanchez-Gomez, E., y Mélia, D. S., Decharme, B., Cassou, C., Sénési, S., Valcke, S., Beau, I., Alias, A., and Chevallier, M.: The CNRM-CM5. 1 global climate model: description and basic evaluation, Climate Dynamics, 40, 2091-2121, 2013.

615 Volodin, E. M., Dianskii, N. A., and Gusev, A. V.: Simulating present-day climate with the INMCM4.0 coupled model of the atmospheric and oceanic general circulations, Izv Atmos Ocean Phy+, 46, 414-431, 10.1134/S000143381004002x, 2010.

Wang, K., and Dickinson, R. E.: Global atmospheric downward longwave radiation at the surface from ground-based observations, satellite retrievals, and reanalyses, Reviews of Geophysics, 51, 150-185, 2013.

Wang, K.: Measurement biases explain discrepancies between the observed and simulated decadal variability of surface
620   incident solar radiation, Sci Rep-Uk, 4, 6144, 2014.

Wang, Y., Zhang, X., Sun, J., Zhang, X., Che, H., and Li, Y.: Spatial and temporal variations of the concentrations of PM 10,
PM 2.5 and PM 1 in China, Atmospheric Chemistry and Physics, 15, 13585-13598, 2015.

Wild, M., Ohmura, A., and Makowski, K.: Impact of global dimming and brightening on global warming, Geophysical
Research Letters, 34, 10.1029/2006gl028031, 2007.

625   Wild, M.: Global dimming and brightening: A review, Journal of Geophysical Research: Atmospheres, 114, 2009.

Wu, G. X., Liu, Y. M., He, B., Bao, Q., Duan, A. M., and Jin, F. F.: Thermal Controls on the Asian Summer Monsoon, Sci
Rep-Uk, 2, ARTN 40410.1038/srep00404, 2012.

Wu, G. X., Duan, A. M., Liu, Y. M., Mao, J. Y., Ren, R. C., Bao, Q., He, B., Liu, B. Q., and Hu, W. T.: Tibetan Plateau climate
dynamics: recent research progress and outlook, Natl Sci Rev, 2, 100-116, 10.1093/nsr/nwu045, 2015.

630   Wu, T., Yu, R., Zhang, F., Wang, Z., Dong, M., Wang, L., Jin, X., Chen, D., and Li, L.: The Beijing Climate Center atmospheric
general circulation model: description and its performance for the present-day climate, Climate dynamics, 34, 123, 2010.

Xie, H., and Zhu, X.: Reference evapotranspiration trends and their sensitivity to climatic change on the Tibetan Plateau (1970–
2009), Hydrol Process, 27, 3685-3693, 2013.

Xie, H., Zhu, X., and Yuan, D. Y.: Pan evaporation modelling and changing attribution analysis on the Tibetan Plateau (1970-
635   2012), Hydrol Process, 29, 2164-2177, 10.1002/hyp.10356, 2015.

Xu, X. D., Lu, C. G., Ding, Y. H., Shi, X. H., Guo, Y. D., and Zhu, W. H.: What is the relationship between China summer
precipitation and the change of apparent heat source over the Tibetan Plateau?, Atmos Sci Lett, 14, 227-234, 10.1002/asl2.444,
2013.

Yang, K., Koike, T., and Ye, B.: Improving estimation of hourly, daily, and monthly solar radiation by importing global data
640   sets, Agricultural and Forest Meteorology, 137, 43-55, 2006.

Yang, K., Ding, B. H., Qin, J., Tang, W. J., Lu, N., and Lin, C. G.: Can aerosol loading explain the solar dimming over the
Tibetan Plateau?, Geophysical Research Letters, 39, Artn L2071010.1029/2012gl053733, 2012.

Yang, K., Wu, H., Qin, J., Lin, C. G., Tang, W. J., and Chen, Y. Y.: Recent climate changes over the Tibetan Plateau and their
impacts on energy and water cycle: A review, Global Planet Change, 112, 79-91, 10.1016/j.gloplacha.2013.12.001, 2014.

645   Yao, T., Pu, J., Lu, A., Wang, Y., and Yu, W.: Recent glacial retreat and its impact on hydrological processes on the Tibetan
Plateau, China, and surrounding regions, Arctic, Antarctic, and Alpine Research, 39, 642-650, 2007.

Yao, T., Xue, Y., Chen, D., Chen, F., Thompson, L., Cui, P., Koike, T., Lau, W. K.-M., Lettenmaier, D., and Mosbrugger, V.:
Recent Third Pole's rapid warming accompanies cryospheric melt and water cycle intensification and interactions between
monsoon and environment: multi-disciplinary approach with observation, modeling and analysis, Bulletin of the American
650   Meteorological Society, 2018.

Yasunari, T.: GEWEX-related Asian monsoon experiment (GAME), Advances in space research, 14, 161-165, 1994.

You, Q., Sanchez-Lorenzo, A., Wild, M., Folini, D., Fraedrich, K., Ren, G., and Kang, S.: Decadal variation of surface solar radiation in the Tibetan Plateau from observations, reanalysis and model simulations, Climate Dynamics, 40, 2073-2086, 2013.

You, Q. L., Kang, S. C., Pepin, N., Flugel, W. A., Sanchez-Lorenzo, A., Yan, Y. P., and Zhang, Y. J.: Climate warming and
655   associated changes in atmospheric circulation in the eastern and central Tibetan Plateau from a homogenized dataset, Global Planet Change, 72, 11-24, 10.1016/j.gloplacha.2010.04.003, 2010.

Yukimoto, S., ADACHI, Y., HOSAKA, M., SAKAMI, T., YOSHIMURA, H., HIRABARA, M., TANAKA, T. Y., SHINDO, E., TSUJINO, H., and DEUSHI, M.: A New Global Climate Model of the Meteorological Research Institute: MRI-CGCM3— Model Description and Basic Performance—, Journal of the Meteorological Society of Japan, 90, 23-64, 2012.

660   Zeng, Z., Piao, S., Li, L. Z. X., Zhou, L., Ciais, P., Wang, T., Li, Y., Lian, X., Wood, E. F., Friedlingstein, P., Mao, J., Estes, L. D., Myneni, Ranga B., Peng, S., Shi, X., Seneviratne, S. I., and Wang, Y.: Climate mitigation from vegetation biophysical feedbacks during the past three decades, Nature Climate Change, 7, 432-436, 10.1038/nclimate3299, 2017.

Zhang, X., Liang, S., Wild, M., and Jiang, B.: Analysis of surface incident shortwave radiation from four satellite products, Remote Sensing of Environment, 165, 186-202, 2015.

665   Zhang, X., Liang, S., Wang, G., Yao, Y., Jiang, B., and Cheng, J.: Evaluation of the Reanalysis Surface Incident Shortwave Radiation Products from NCEP, ECMWF, GSFC, and JMA Using Satellite and Surface Observations, Remote Sensing, 8, 225, 2016.

Zhou, C., Wang, K., and Qi, D.: Attribution of the July 2016 Extreme Precipitation Event Over China's Wuhang, Bulletin of the American Meteorological Society, 99, S107-S112, 2018.

670

Table 1: Summary of the Coupled Model Intercomparison Project Phase 5 (CMIP5) surface downward radiation simulations used in this study.

Name	Spatial Resolution		Reference
	Longitude	**Latitude**	
CMCC-CM	0.75°	0.75°	Scoccimarro et al. (2011)
CESM1-CAM5	1.25°	0.94°	Meehl et al. (2013)
CESM1-BGC	1.25°	0.94°	Long et al. (2013)
CCSM4	1.25°	0.94°	Gent et al. (2011)
MRI-CGCM3	1.13°	1.13°	Yukimoto et al. (2012)
BCC-CSM1.1m	1.13°	1.13°	Wu et al. (2010)
MIROC5	1.41°	1.41°	Mochizuki et al. (2012)
CNRM-CM5	1.41°	1.41°	Voldoire et al. (2013)
ACCESS1.0	1.88°	1.24°	Franklin et al. (2013)
ACCESS1.3	1.88°	1.24°	Franklin et al. (2013)
IPSL-CM5A-MR	2.50°	1.26°	Dufresne et al. (2013)
INMCM4	2.00°	1.50°	Volodin et al. (2010)
MPI-ESM-LR	1.88°	1.88°	Jungclaus et al. (2010)
MPI-ESM-MR	1.88°	1.88°	Jungclaus et al. (2010)
CSIRO-Mk3.6.0	1.88°	1.88°	Gordon et al. (2010)
CMCC-CMS	1.88°	1.88°	Scoccimarro et al. (2011)
NorESM1-M	2.50°	1.88°	Tjiputra et al. (2013)
NorESM1-ME	2.50°	1.88°	Tjiputra et al. (2013)

675

Table 2: Meta information on the satellite and reanalysis products. All products were resampled into 1 Lat/Lon degree using bilinear interpolation or spatial averaging in the paper. All data were accessed on 15 December 2018.

Variable	Version	Time Span	Spatial Resolution	Data Availability	Usage
DSR	CERES EBAF-surface Ed4.0	2001.01–2015.12	1°×1°	https://ceres.larc.nasa.gov/order_data.php	calibration
DLR	CERES EBAF-surface Ed4.0	2001.01–2015.12	1°×1°	https://ceres.larc.nasa.gov/order_data.php	calibration
TOA albedo	CERES TOA-surface Ed4.0	2001.01–2015.12	1°×1°	https://ceres.larc.nasa.gov/order_data.php	attribution & depressing effect
AOD	MOD/MYD08 C6.1	2001.01–2015.12	1°×1°	https://earthengine.google.com/	attribution
AOD	SeaWIFS 1.0_L3M	1998.01–2010.12	1°×1°	https://disc.gsfc.nasa.gov/datasets?page=1	attribution
aerosol index	TOMS & OMI Aerosol Index L3	1980.01–1993.12, 1997.01–2015.12	1°×1.25°	https://disc.gsfc.nasa.gov/datasets?page=1	attribution
PM 2.5	Global Annual PM2.5 Grids from MODIS, MISR and SeaWiFS AOD, v1	2000.01–2015.12	0.01°×0.01°	http://fizz.phys.dal.ca/~atmos/martin/?page_id=140	attribution
dust	MERRA2	2000.01–2015.12	0.5°×0.625°	https://disc.gsfc.nasa.gov/datasets?page=1	attribution
cloud fraction	MOD/MYD08 C6.1	2001.01–2015.12	1°×1°	https://earthengine.google.com/	attribution
cloud fraction	Corrected ISCCP and PATMOS-X monthly cloud fraction	1984.01–2007.12	1°×1°	https://rda.ucar.edu/datasets/ds741.5/	attribution
TOA ASR	DEEP-C TOA _ASR v02	1985.01–2015.12	1°×1°	http://www.met.reading.ac.uk/~sgs02rpa/research/DEEP-C/	attribution

albedo	GLASS albedo V05	2001.01–2015.12	0.05°×0.05°	http://glass-product.bnu.edu.cn	depressing effect
surface emissivity	ASTER_GED v4.1	2001.01–2015.12	0.05°×0.05°	https://lpdaac.usgs.gov/dataset_discovery/community/community_products_table/ag5kmmoh_v041	depressing effect

Variables: DSR, downward shortwave radiation; DLR, downward longwave radiation; TOA albedo, top of atmosphere albedo; AOD, aerosol optical depth; PM2.5, Particulate matter 2.5; ASR, absorbed solar radiation. Products' name are illustrated in the
680 **Section 2.**
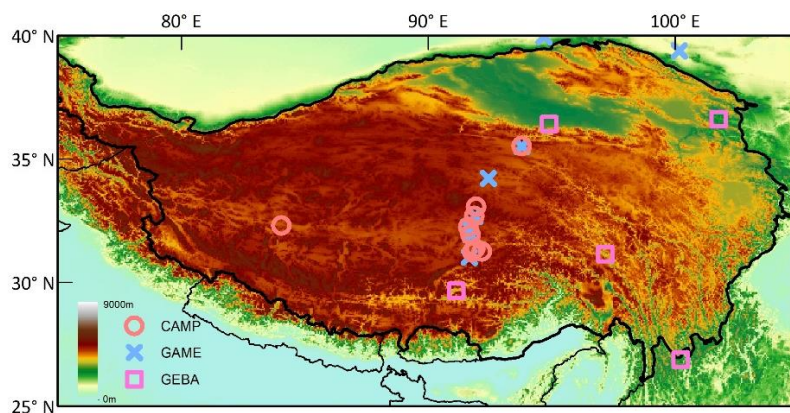
Figure 1: Site distribution. Observations from three ground networks (Global Energy and Water Exchanges [GEWEX] Asian
Monsoon Experiment [GAME], Coordinated Energy and Water Cycle Observation Project [CEOP] Asia-Australia Monsoon
Project [CAMP], and Global Energy Balance Archive [GEBA]) are from 1960–2005. Vector layer data is free for academic use
licensed by Database of Global Administrative Areas (GADM). Elevation data is provided by National Oceanic and Atmospheric
Administration (NOAA) (GLOBE).

685
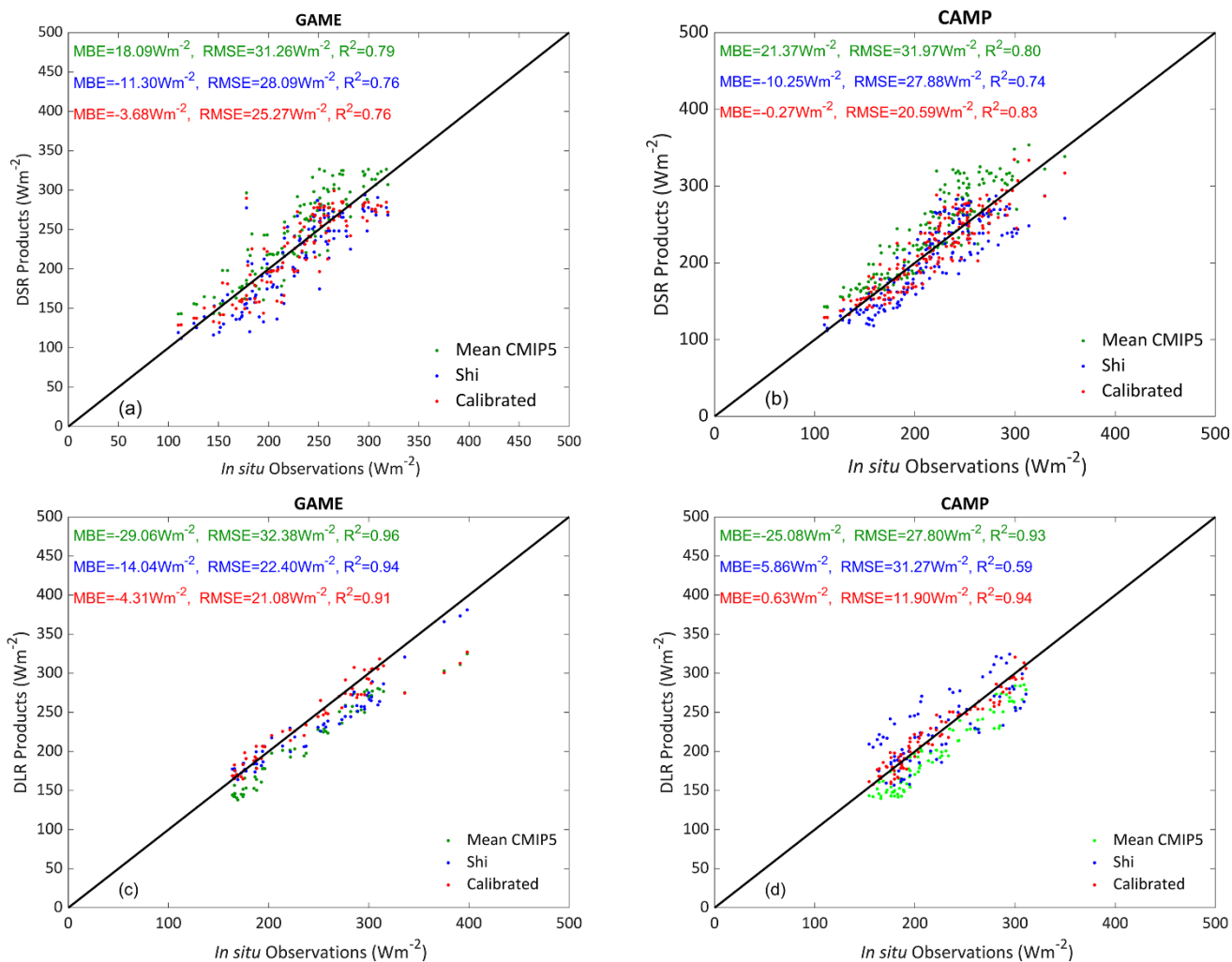
Figure 2: Scatterplot of site validation results from two ground networks: (a, b) downward shortwave radiation (DSR), (c, d) downward longwave radiation (DLR).
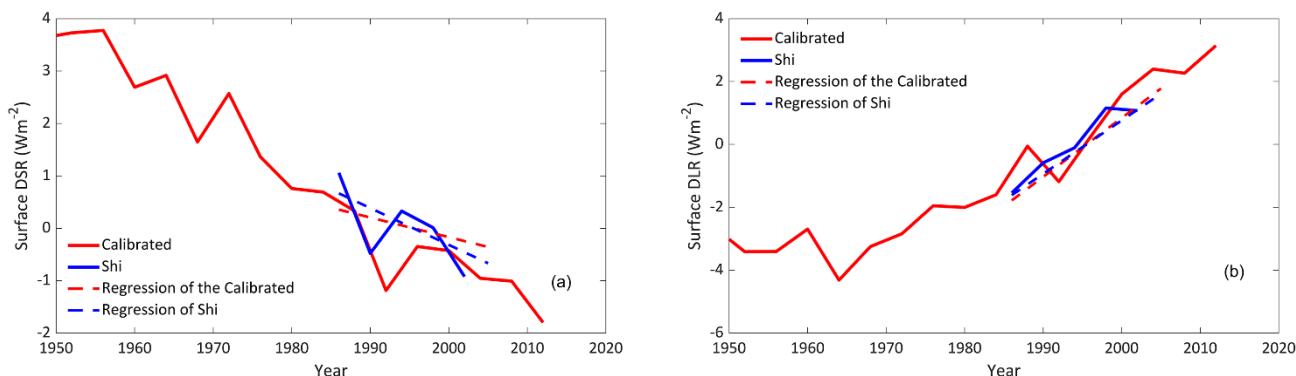
Figure 3: Trend comparison between calibrated downward radiation datasets and Shi and Liang (2013). Temporal variations over the Tibetan Plateau (TP) in (a) and (b) were averaged by the 5-year moving window in order to remove the impact of annual variability.
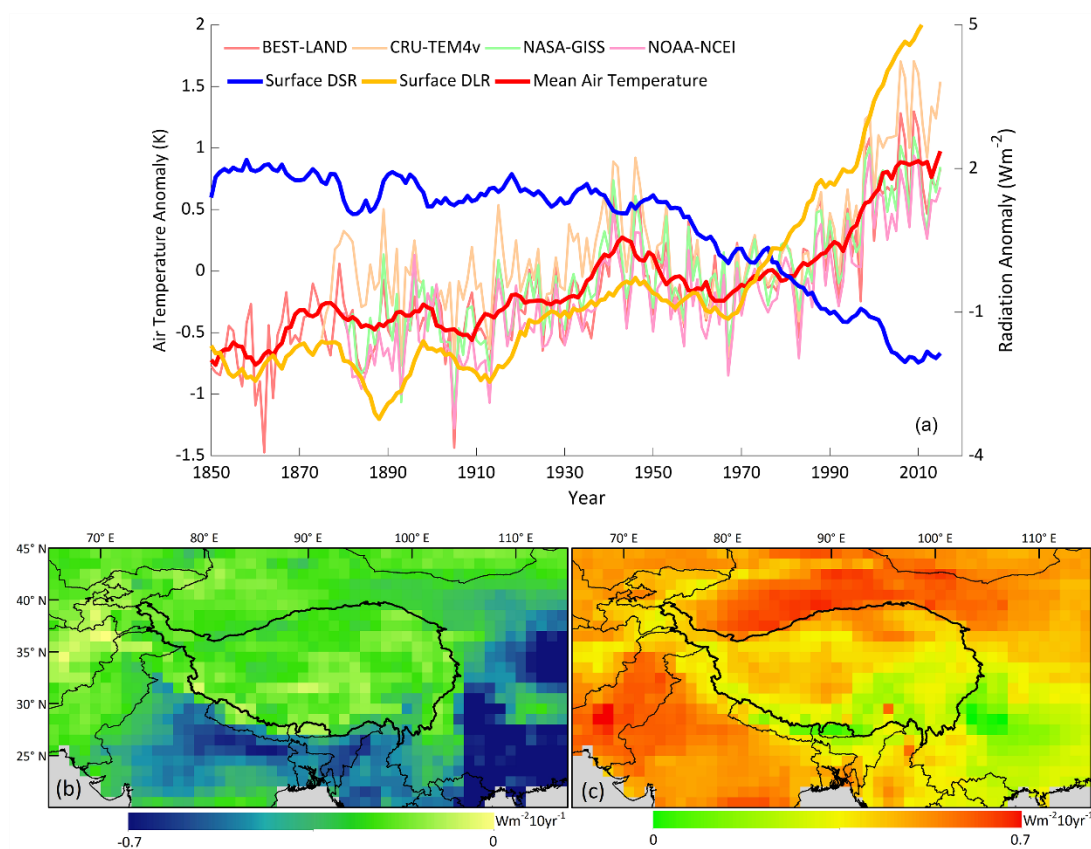
Figure 4: Spatiotemporal variations in surface downward shortwave radiation (DSR) and downward longwave radiation (DLR) over the Tibetan Plateau (TP) and its neighboring regions from 1850 to 2015. Temporal variations in (a) were averaged by the 10-year moving window in order to remove the impact of annual variability. The trends of DSR (b) and DLR (c) are significant, with p-values < 0.01. Vector layer data is free for academic use licensed by GADM.
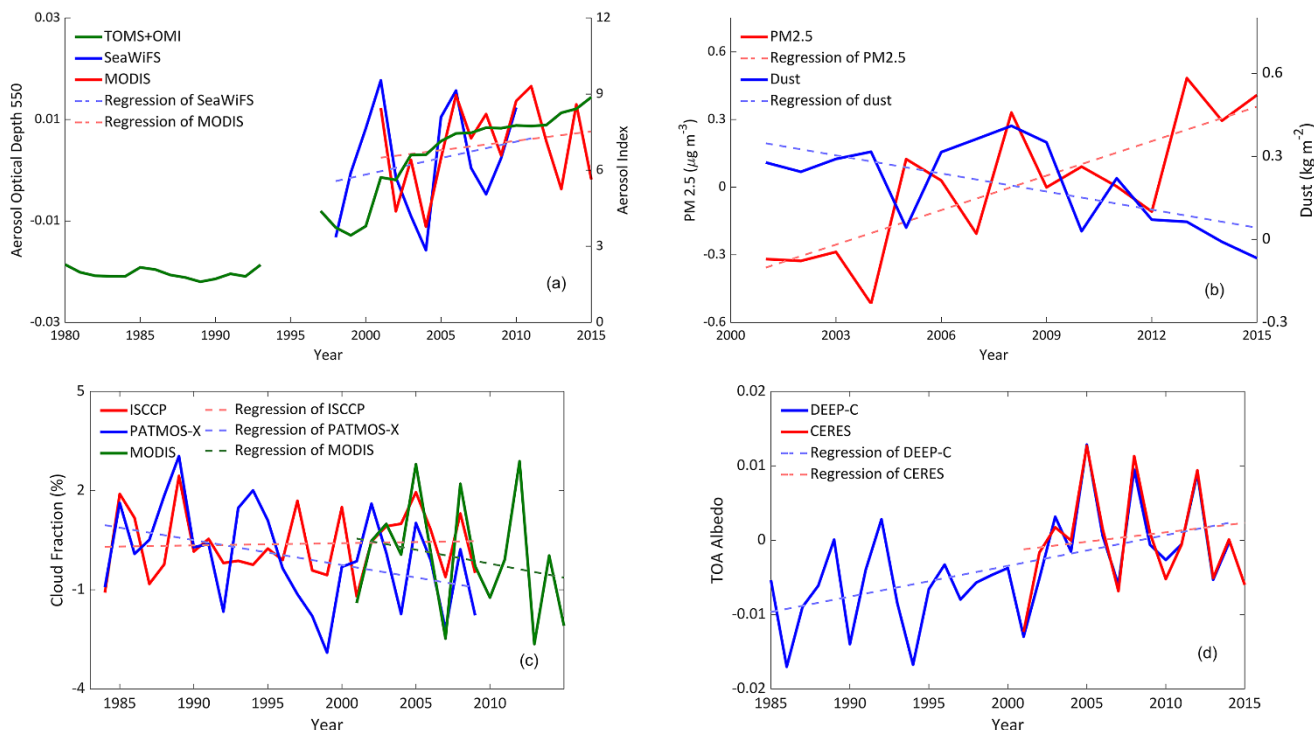
Figure 5: Temporal variation in detected factors from remote sensing products over the Tibetan Plateau (TP): (a) aerosol optical depth (AOD) and aerosol index, (b) Particulate matter (PM)2.5 and dust, (c) cloud fraction, and (d) top-of-atmosphere (TOA) albedo.

705
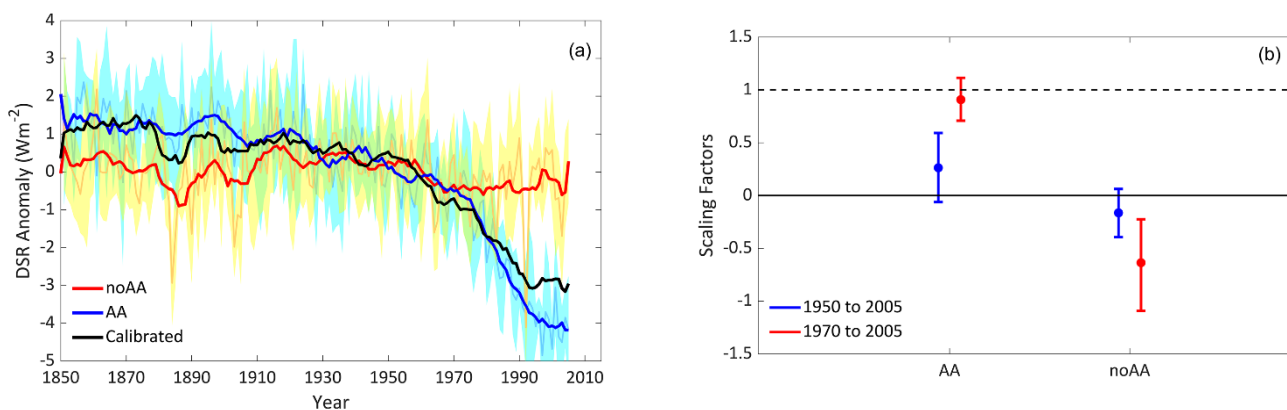
Figure 6: (a) Temporal variations of the calibrated, anthropogenic aerosol–driven (AA-driven) and noAA-driven DSR. Temporal variations were averaged by a 10-year moving window to remove the impact of annual variability. (b) Scaling factors of the AA and noAA forcing simulation on downward shortwave radiation (DSR).
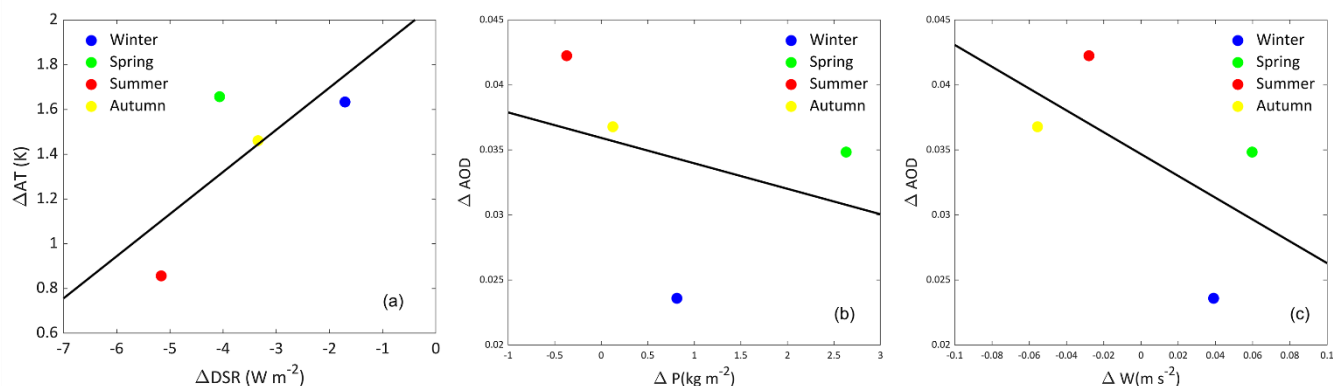
710

Figure 7: Relationships between variable changes at the seasonal scale from 1850 to 2015: (a) the decrease in downward shortwave radiation (DSR) and increase in air temperature, (b) precipitation change and aerosol optical depth (AOD) increase, (c) wind speed change and AOD increase.
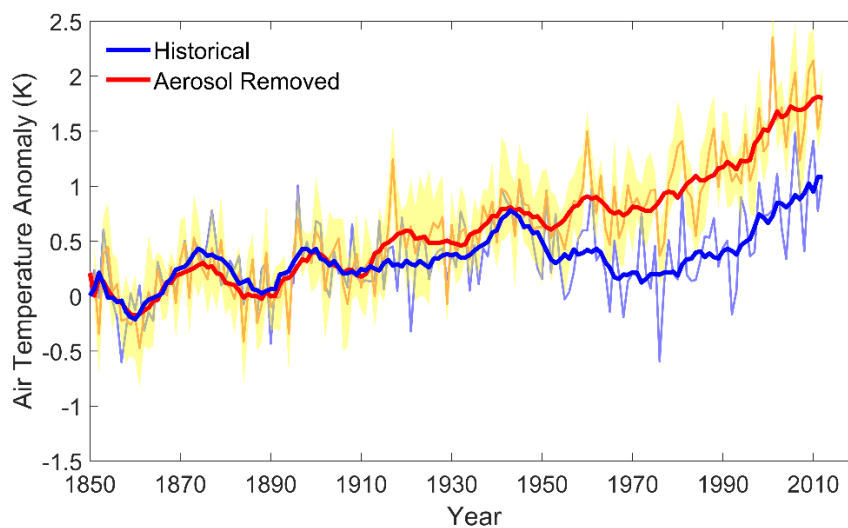
715 **Figure 8: Temporal annual variation in air temperature, and air temperature with the depressing effect of aerosols removed in the summer season.**